Universität des Saarlandes

Mathematical Foundations and Generalisations of the Census Transform for Robust Optic Flow Computation

David Hafner, Oliver Demetz,
Joachim Weickert and Martin Reißel

Mathematical Foundations and Generalisations of the Census Transform for Robust Optic Flow Computation

David Hafner

Mathematical Image Analysis Group,
Faculty of Mathematics and Computer Science,
Saarland University, Campus E1.7, 66041 Saarbrücken, Germany
hafner@mia.uni-saarland.de

Oliver Demetz

Mathematical Image Analysis Group,
Faculty of Mathematics and Computer Science,
Saarland University, Campus E1.7, 66041 Saarbrücken, Germany
demetz@mia.uni-saarland.de

Joachim Weickert

Mathematical Image Analysis Group,
Faculty of Mathematics and Computer Science,
Saarland University, Campus E1.7, 66041 Saarbrücken, Germany
weickert@mia.uni-saarland.de

Martin Reißel

Fachbereich Medizintechnik und Technomathematik,
Standort Jülich, Fachhochschule Aachen,
Heinrich-Mußmann-Straße 1, 52428 Jülich, Germany
reissel@fh-aachen.de

Abstract

In recent years, the popularity of the census transform has grown rapidly. It provides features that are invariant under monotonically increasing intensity transformations. Therefore, it is exploited as a key ingredient of various computer vision problems, in particular for illumination-robust optic flow models. However, despite being extensively applied, its underlying mathematical foundations are not well-understood so far. The main contributions of our paper are to provide these missing insights, and in this way to generalise the concept of the census transform. To this end, we transfer the inherently discrete transform to the continuous setting and embed it into a variational framework for optic flow estimation. This uncovers two important properties: the strong reliance on local extrema and the induced anisotropy of the data term by acting along isolines. These findings open the door to generalisations of the census transform that are not obvious in the discrete formulation. To illustrate this, we introduce and analyse second-order census models that are based on thresholding the second directional derivatives. Last but not least, we constitute links of census-based approaches to established data terms such as gradient constancy, Hessian constancy, and Laplacian constancy, and we confirm our findings by means of experiments.

1   Introduction

The census transform is a classical neighbourhood descriptor that has been proposed by Zabih and Woodfill in 1994 [48]. It computes for every pixel a binary string (*census signature*) by comparing its grey value with the grey values in its neighbourhood. The census signature yields the value 0 if the neighbour is smaller than the reference pixel, and 1 otherwise. Figure 1 illustrates the census transform with a 3×3 intensity patch. The resulting signature string has length 8 and thus, can be represented efficiently by a single byte.

4	4	65
3	25	14
83	15	88

0	0	1
0		0
1	0	1

01000101

Intensity values   Census digits   Census signature
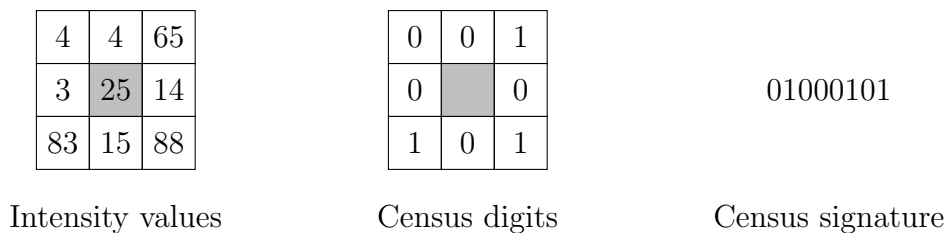
Figure 1: Census transform with a 3×3 neighbourhood patch. A census digit is 0 if the corresponding neighbour is smaller than the central pixel (marked in grey) and 1 otherwise. The final census signature contains all census digits, where we start with the right neighbour and proceed counter-clockwise.

The key property that makes the census transform attractive for the computer vision community is its robustness under illumination changes. Whenever one tries to establish a correspondence relation over multiple frames, any changes in appearance create a big challenge. A particular example is the computation of displacement fields (*optic flow*) in real-world image sequences, where illumination changes are omnipresent. Such a robustness against illumination changes plays a literally vital role in driver assistant systems;

1

see for instance Rabe [33]. Here the census transform is very beneficial and frequently used. By construction, its signatures are *morphologically invariant*, i.e. invariant under global monotonically increasing grey level rescalings. Stein [37] uses the census signatures in an efficient feature matching approach. A hash table-based indexing scheme provides flow estimates in real-time and is well-suited for large displacements. Müller et al. [25] as well as Mohamed and Mertsching [23] exploit these sparse feature matches to handle large displacements and to recover image details lost in a coarse-to-fine minimisation technique, respectively. Furthermore, Müller et al. [24] embed the census transform as data term into a variational optic flow framework. Tests in real-world scenarios demonstrate the desired morphological invariance of the resulting dense flow fields. Vogel et al. [43] compare different data terms and show that the census transform is well-suited for challenging lightning conditions. Also in the context of stereo estimation, Mei et al. [21] and Ranftl et al. [34] have illustrated the usefulness of the census transform. Other applications of the census transform include face recognition problems [9]. In spite of its successful applications, however, the theoretical understanding of the census transform is still rather limited.

1.1 Our Contributions

The goal of our paper is to provide a thorough theoretical foundation of the census transform and extend it to more general formulations. It is based on our SSVM 2013 conference publication [13] where three contributions are established:

 (i) Differences to neighbours are regarded as approximations of directional derivatives, and the continuous limit over all possible angles is studied.

 (ii) This concept is developed into a constancy assumption and embedded as data term in a variational model for optic flow computation.

(iii) The energy functional and its minimisation are analysed in order to obtain a novel interpretation of census-based optic flow. This interpretation uncovers highly interesting properties of the census transform that have not been used in other optic flow formulations.

Our present journal paper extends these results in several aspects. In particular, we introduce the following main contributions:

(iv) We generalise the census idea such that it includes also higher order directional derivatives.

 (v) We present detailed proofs of the theorems that we apply in our mathematical analysis of census-based optic flow approaches.

(vi) The first and second order variants of the census transform are juxtaposed experimentally such that their individual advantages and limitations are made explicit.

We want to stress that the focus of our work is not on developing new competitive high-end optic flow methods: We are interested in the mathematical foundations and generalisations of census-based approaches. Once their properties are well-understood, these ideas can easily be embedded in any highly sophisticated optic flow method that ranks favourably in the Middlebury [1] or KITTI benchmark [10].

1.2 Related Work

Since 1994, census-like ideas have appeared under several names in the literature: Ojala et al. [28] developed a closely related concept and interpreted the resulting descriptor as a binary number (*local binary patterns*). Later Calonder et al. [5] revisited this idea by introducing the feature point descriptor *BRIEF*. In the meantime the concept of local binary patterns has found numerous applications in pattern recognition and computer vision; for an overview we refer to the book of Pietikäinen et al. [31] and the references therein.

There is also a long tradition of designing methods for illumination-robust optic flow computation, either by introducing robust features or by modelling the illumination changes explicitly.

The use of brightness gradient constancy renders the optic flow model robust w.r.t. global additive brightness changes. It goes back to Nagel [26], Tretiak and Pastor [39], and Uras et al. [40], while embeddings in a variational setting have been studied e.g. by Schnörr [36] and Brox et al. [3]. In contrast to additive changes, Steinbrücker et al. [38] achieve an invariance against multiplicative illumination changes via a patch-based data term using normalised cross correlation. Wedel et al. [44] preform a so-called structure-texture decomposition of the input images by means of the image denoising method by Rudin et al. [35]. The textural part shows an increased robustness under shadows and shading reflections. Another idea by van de Weijer and Gevers [41] as well as Mileva et al. [22] is to make use of photometric invariants to design illumination-robust flow methods for colour images. Also the mutual information [42] turns out to be a useful feature for registering images with different illumination; see Hermosillo et al. [16] and Panin [29]. In order to extract the maximal amount of information from a local neighbourhood while providing a morphological invariance, Demetz et al. [8] introduce the *complete rank transform* in a variational optic flow setting.

Instead of matching illumination-robust features, the following approaches follow a different idea to tackle brightness changes: They model them explicitly. Based on *comparagrams* [20], Kim and Pollefeys [18] as well as Dederscheck et al. [7] estimate the *brightness transfer function* that allows to compensate for global brightness changes. In order to handle also local changes, the model of Cornelius and Kanade [6] allows smooth additive variations from the brightness constancy assumption. Negahdaripour [27] extends this idea and presents a general variational framework that optimises w.r.t. spatially varying multiplicative and additive illumination changes in addition to the optic flow field. Hager and Belhumeur [14] apply a principal component analysis to set up the basis of a parameterised illumination model whose parameters are jointly computed with the motion. In this context, Haussecker and Fleet [15] propose to estimate physically-based parameters that are intended to model the illumination variations more accurately. Kim and Kak [19] compare different local and global approaches under brightness changes and in particular improve the robustness against noise.

1.3 Paper Organisation

Starting with a continuous interpretation of the census transform, Section 2 presents our census-based variational optic flow method. The energy formulation and its minimisation

yield new insights into census-based approaches. These results are presented in Section 3. The uncovered insights allow us to extend the census idea to higher order (Section 4). After having sketched our numerical algorithm in Section 5, we evaluate the proposed method in Section 6. Finally, Section 7 concludes the paper with a summary and an outlook.

2 Census-Based Variational Optic Flow

In this section, we introduce our census-based optic flow method. To this end, we start with a formal definition of the original census transform and derive the corresponding constancy assumption in a continuous manner. This provides the basis of our energy functional and is the starting point of our analysis.

2.1 Census Transform

Let in a discrete setting $g_{i,j}$ denote the grey values of an image. Then, every digit of the census signature in pixel $(i,j)^\top$ is computed as

$$H\left(g_{i+d_1,j+d_2} - g_{i,j}\right), \tag{1}$$

where $(i+d_1, j+d_2)^\top$ represents a neighbouring pixel, and $H\colon \mathbb{R} \to \{0,1\}$ denotes the Heaviside step function

$$H(z) := \begin{cases} 0 & \text{if } z < 0, \\ 1 & \text{if } z \geq 0. \end{cases} \tag{2}$$

2.2 Census-Based Constancy Assumption

Let us now transfer the census transform to the continuous setting and derive the associated constancy assumption. We denote an image sequence by a function $f(x,y,t)$ where $(x,y)^\top$ describes the location within the rectangular image domain $\Omega \subset \mathbb{R}^2$ and $t \in [0,T]$ is the time.

The argument of the step function in Equation 1 approximates a directional derivative. Consequently, one census digit can be interpreted as the discrete version of

$$H\left(\boldsymbol{e}_\varphi^\top \boldsymbol{\nabla} f(x,y,t)\right), \tag{3}$$

where the unit vector $\boldsymbol{e}_\varphi := (\cos\varphi, \sin\varphi)^\top$ specifies the direction, and the gradient operator $\boldsymbol{\nabla} := (\partial_x, \partial_y)^\top$ only acts on the spatial domain. To ensure the differentiability of f, we presmooth the input images by a convolution with a Gaussian.

Let us now derive the constancy constraint based on the assumption that two corresponding points $(x,y,t)^\top$ and $(x+u, y+v, t+1)^\top$ in consecutive frames have identical census signatures. In our notation, the functions $u, v\colon \Omega \to \mathbb{R}$ represent the sought optic flow components. Considering all angles $\varphi \in [0, 2\pi)$, the constancy assumption of the census signature implies

$$H\left(\boldsymbol{e}_\varphi^\top \boldsymbol{\nabla} f(x+u, y+v, t+1)\right) - H\left(\boldsymbol{e}_\varphi^\top \boldsymbol{\nabla} f(x,y,t)\right) \overset{!}{=} 0. \tag{4}$$

4
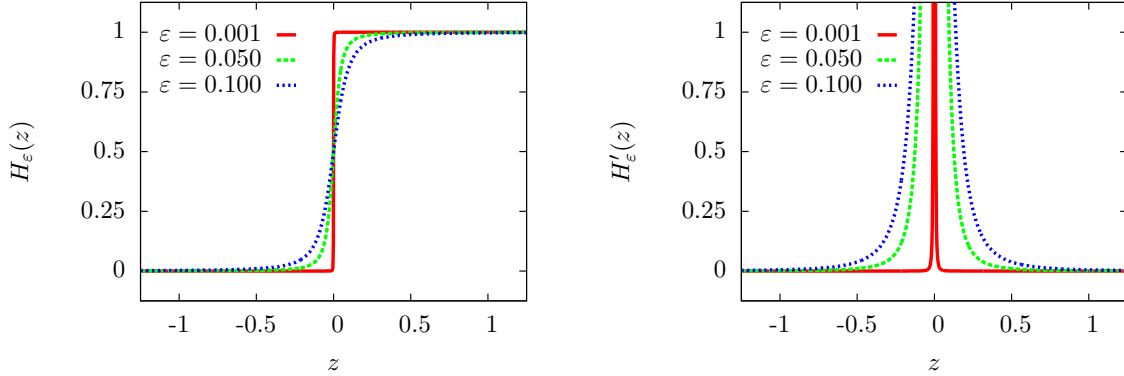
Figure 2: Different approximations $H_\varepsilon(z)$ of the Heaviside step function (*left*) and corresponding derivatives $H'_\varepsilon(z)$ (*right*). Smaller choices of ε lead to closer approximations of the original sharp step function.

In order to embed this constraint as data term in an energy functional, we consider a linearised version of it. To this end, we replace the Heaviside step function H by the smooth approximation

$$H_\varepsilon(z) \; := \; \frac{1}{2}\left(1 + \frac{z}{\sqrt{z^2 + \varepsilon^2}}\right),$$ (5)

with a small positive regularisation parameter ε that satisfies $\varepsilon \geq \varepsilon_0 > 0$ (cf. Figure 2). The lower bound ε_0 ensures that ε is also in the limit strictly larger than 0. Otherwise, the linearisation becomes invalid and the resulting data term would not be suitable for a typical variational optic flow framework [17].

Assuming small flow components u and v as well as a small change of the temporal derivative of a census digit, we propose the following linearisation: With the derivative of the regularised step function

$$H'_\varepsilon(z) \; = \; \frac{\varepsilon^2}{2\left(z^2 + \varepsilon^2\right)^{3/2}},$$ (6)

linearising the regularised version of the constraint (4) around $(x, y, t)^\top$ yields

$$H'_\varepsilon\big(\boldsymbol{e}_\varphi^\top \boldsymbol{\nabla} f\big) \; \cdot \; \boldsymbol{e}_\varphi^\top \big(\underbrace{\boldsymbol{\nabla} f_x \cdot u + \boldsymbol{\nabla} f_y \cdot v + \boldsymbol{\nabla} f_t}_{\boldsymbol{p}_{uv}}\big) \; \overset{!}{=} \; 0.$$ (7)

For the sake of readability, we omit here the argument $(x, y, t)^\top$ of f. Further, the term $\boldsymbol{\nabla} f_x \cdot u + \boldsymbol{\nabla} f_y \cdot v + \boldsymbol{\nabla} f_t$ represents the widely-used linearised gradient constancy expression [3, 26, 36, 39, 40] and is in the following abbreviated by $\boldsymbol{p}_{uv}$.

2.3 Energy Formulation and Minimisation

As a next step, we embed the derived census constancy assumption into a variational framework. The corresponding energy reads

$$E(u, v) \; := \; \int_\Omega \big(M(u, v) + \alpha \cdot S(\boldsymbol{\nabla} u, \boldsymbol{\nabla} v)\big) \, \mathrm{d}x \, \mathrm{d}y,$$ (8)

5

with the quadratic census-based data term

$$M(u,v) := \frac{1}{\pi} \int_0^{2\pi} \left(H'_\varepsilon \left(\boldsymbol{e}_\varphi^\top \boldsymbol{\nabla} f \right) \cdot \boldsymbol{e}_\varphi^\top \boldsymbol{p}_{uv} \right)^2 \, \mathrm{d}\varphi \tag{9}$$

and the homogeneous smoothness term [17]

$$S(\boldsymbol{\nabla} u, \boldsymbol{\nabla} v) := |\boldsymbol{\nabla} u|^2 + |\boldsymbol{\nabla} v|^2 \,. \tag{10}$$

The positive regularisation parameter α allows to steer the impact of the data and smoothness term, respectively.

Following the calculus of variations [11], the minimiser of the energy in Equation 8 w.r.t. u and v has to fulfil the Euler-Lagrange equations

$$\frac{1}{\pi} \int_0^{2\pi} H'^2_\varepsilon (\boldsymbol{e}_\varphi^\top \boldsymbol{\nabla} f) \cdot \boldsymbol{e}_\varphi^\top \boldsymbol{\nabla} f_x \cdot \boldsymbol{e}_\varphi^\top \boldsymbol{p}_{uv} \, \mathrm{d}\varphi \;-\; \alpha \, \Delta u \;=\; 0 \,, \tag{11}$$

$$\frac{1}{\pi} \int_0^{2\pi} H'^2_\varepsilon (\boldsymbol{e}_\varphi^\top \boldsymbol{\nabla} f) \cdot \boldsymbol{e}_\varphi^\top \boldsymbol{\nabla} f_y \cdot \boldsymbol{e}_\varphi^\top \boldsymbol{p}_{uv} \, \mathrm{d}\varphi \;-\; \alpha \, \Delta v \;=\; 0 \,, \tag{12}$$

with homogeneous Neumann boundary conditions

$$\boldsymbol{n}^\top \boldsymbol{\nabla} u \;=\; 0 \quad \text{on } \partial\Omega, \tag{13}$$

$$\boldsymbol{n}^\top \boldsymbol{\nabla} v \;=\; 0 \quad \text{on } \partial\Omega, \tag{14}$$

where $\boldsymbol{n}$ denotes the outer normal vector to the boundary $\partial\Omega$ of the image domain Ω.

3 Interpretation

Let us now analyse the presented census-based data term in Equation 9. After some small algebraic rearrangements we can rewrite it as quadratic form

$$M(u,v) \;=\; \boldsymbol{p}_{uv}^\top \boldsymbol{C} \boldsymbol{p}_{uv} \tag{15}$$

with a symmetric *census tensor* $\boldsymbol{C} \in \mathbb{R}^{2\times 2}$ that is given by

$$\boldsymbol{C} := \frac{1}{\pi} \int_0^{2\pi} H'^2_\varepsilon (\boldsymbol{e}_\varphi^\top \boldsymbol{\nabla} f) \cdot \boldsymbol{e}_\varphi \boldsymbol{e}_\varphi^\top \, \mathrm{d}\varphi \,. \tag{16}$$

An analysis of a closely related tensor has already been performed by Weickert [45] in the context of anisotropic diffusion filtering. However, since we need some adaptations in the notations and since the proofs in [45] are only briefly sketched, we review the relevant results below, and we present full proofs in the appendix.

Let $(r,\psi)^\top$ denote the polar coordinates of $\boldsymbol{\nabla} f \neq \boldsymbol{0}$. Then the eigenvectors of $\boldsymbol{C}$ are parallel and perpendicular to the isolines of f, respectively. They are given by

$$\boldsymbol{w}_\parallel(\psi) \;=\; \frac{\boldsymbol{\nabla} f^\perp}{|\boldsymbol{\nabla} f|} \;=\; \begin{pmatrix} -\sin\psi \\ \cos\psi \end{pmatrix} \,, \tag{17}$$

$$\boldsymbol{w}_\perp(\psi) \;=\; \frac{\boldsymbol{\nabla} f}{|\boldsymbol{\nabla} f|} \;=\; \begin{pmatrix} \cos\psi \\ \sin\psi \end{pmatrix} \,, \tag{18}$$

with corresponding eigenvalues

$$\lambda_{\parallel}(r) \;=\; \frac{4}{\pi} \int_0^{\pi/2} H_{\varepsilon}'^{\,2}\,(r \cdot \cos\varphi) \cdot \sin^2\varphi\,\mathrm{d}\varphi\,, \tag{19}$$

$$\lambda_{\perp}(r) \;=\; \frac{4}{\pi} \int_0^{\pi/2} H_{\varepsilon}'^{\,2}\,(r \cdot \cos\varphi) \cdot \cos^2\varphi\,\mathrm{d}\varphi\,. \tag{20}$$

With the eigendecomposition

$$\boldsymbol{C} \;=\; \lambda_{\parallel}(r) \cdot \boldsymbol{w}_{\parallel}(\psi)\,\boldsymbol{w}_{\parallel}^{\top}(\psi) \;+\; \lambda_{\perp}(r) \cdot \boldsymbol{w}_{\perp}(\psi)\,\boldsymbol{w}_{\perp}^{\top}(\psi) \tag{21}$$

the data term (15) can be rewritten as

$$M(u,v) \;=\; \lambda_{\parallel}(r) \cdot \left(\boldsymbol{w}_{\parallel}^{\top}(\psi)\boldsymbol{p}_{uv}\right)^2 \;+\; \lambda_{\perp}(r) \cdot \left(\boldsymbol{w}_{\perp}^{\top}(\psi)\boldsymbol{p}_{uv}\right)^2. \tag{22}$$

This formula decomposes the data term into two orthogonal constraints. It can be understood as a projection of the linearised gradient constancy expression $\boldsymbol{p}_{uv}$ along resp. across the isolines of f. These projections are weighted with the corresponding eigenvalues $\lambda_{\parallel}(r)$ and $\lambda_{\perp}(r)$.

3.1 Anisotropic Data Term

Based on the formulation in Equation 22, the following paragraphs discuss the behaviour of the data term at different image regions.

3.1.1 Vanishing Gradient

At extrema or homogeneous regions $|\boldsymbol{\nabla} f|$ vanishes, i.e. $r \to 0$. In this case, the eigenvalues of the census tensor $\boldsymbol{C}$ fulfil

$$\lim_{r \to 0} \lambda_{\parallel}(r) \;=\; H_{\varepsilon}'^{\,2}(0) \cdot \underbrace{\frac{4}{\pi} \int_0^{\pi/2} \sin^2\varphi\,\mathrm{d}\varphi}_{=1} \;=\; H_{\varepsilon}'^{\,2}(0)\,, \tag{23}$$

$$\lim_{r \to 0} \lambda_{\perp}(r) \;=\; H_{\varepsilon}'^{\,2}(0) \cdot \underbrace{\frac{4}{\pi} \int_0^{\pi/2} \cos^2\varphi\,\mathrm{d}\varphi}_{=1} \;=\; H_{\varepsilon}'^{\,2}(0)\,. \tag{24}$$

Revisiting Equation 6, we see that $H_{\varepsilon}'^{\,2}(0) = 1/4\varepsilon^2$. Hence, both eigenvalues $\lambda_{\parallel}$ and $\lambda_{\perp}$ exceed all bounds for close approximations of the Heaviside function. This means that both components in the data term (22) are very large.

The occurring second order image derivatives $\boldsymbol{e}_{\varphi}^{\top}\boldsymbol{\nabla} f_x$ and $\boldsymbol{e}_{\varphi}^{\top}\boldsymbol{\nabla} f_y$ in the Euler-Lagrange equations (11) and (12) behave differently in local extrema and homogeneous image regions. Consequently, our analysis of the constancy assumption has to differentiate these two cases.

Local Extrema. In local extrema, the first order derivatives of f vanish, but the second order derivatives are in general non-zero. Since the reaction parts of the Euler-Lagrange equations (11)–(12) are weighted with the factor $1/4\varepsilon^2$, they dominate the diffusion terms for small ε.

This reveals a surprising property of the discussed census-based model: The census constancy assumption implicitly enforces a strong reliance on the local extrema. This contributes to the observed morphological invariance: On the one hand the positions of the minima and maxima remain constant under monotonically increasing grey level rescalings, and on the other hand the property $\boldsymbol{\nabla} f = \boldsymbol{0}$ at the extrema is not violated under those illumination changes. Thus, the imposed constancy assumption of the gradient holds here in *all* directions.

Homogeneous Regions. In contrast, the second order image derivatives $\boldsymbol{\nabla} f_x$ and $\boldsymbol{\nabla} f_y$ go to $\boldsymbol{0}$ in homogeneous regions. As a result, the terms $\boldsymbol{e}_\varphi^\top \boldsymbol{\nabla} f_x$ and $\boldsymbol{e}_\varphi^\top \boldsymbol{\nabla} f_y$ in the reaction parts of the Euler-Lagrange equations vanish. Hence, the solution at those regions is solely determined by filling-in the information from the neighbouring pixels:

$$\Delta\, u \;=\; 0 \quad \text{and} \quad \Delta\, v \;=\; 0\,. \tag{25}$$

3.1.2 High Contrast Edges

The previous paragraph was concerned with image regions where $|\boldsymbol{\nabla} f| = r \to 0$. Let us now analyse the opposite case that corresponds to high contrast edges of the image $(r \to \infty)$. Considering the eigenvalues of the census tensor $\boldsymbol{C}$ shows the strong anisotropic behaviour in those regions (cf. [45] and Appendix A.2):

$$\lim_{r \to \infty} \frac{\lambda_\parallel (r)}{\lambda_\perp (r)} \;=\; \infty\,. \tag{26}$$

The informative Equation 22 shows that the constancy of the gradient entries is here strongly imposed along isolines of f. In contrast, the constancy assumption across isolines is weighted down. This anisotropy is, besides the reliance on the local extrema, another reason for the morphological invariance of census-based methods. Under monotonically increasing grey level rescalings, the positions of the isophotes are invariant and additionally the directional derivatives along these isophotes remain zero. In other words, the gradient constancy assumption is valid *along the isolines* of the image.

3.2 Relation to Gradient Constancy Assumption

Let us now illustrate the connection between the presented census-based constancy assumption and the widely-used gradient constancy assumption [3, 26, 36, 39, 40]. The quadratic data term of the linearised gradient constancy assumption reads

$$\left(f_{xx}u + f_{xy}v + f_{xt}\right)^2 + \left(f_{yx}u + f_{yy}v + f_{yt}\right)^2 \;=\; \boldsymbol{p}_{uv}^\top\, \boldsymbol{I}\, \boldsymbol{p}_{uv}\,, \tag{27}$$

where $\boldsymbol{I}$ denotes the 2×2 identity matrix. This formulation inherently decouples the constancy assumptions of the gradient entries f_x and f_y. Comparing the data terms (15) and (27), we observe that the reason for the increased robustness of census-based methods

(compared to gradient constancy) is solely hidden in the census tensor $\boldsymbol{C}$. This confirms our findings from Section 3.1: Coupling the constancy assumptions of f_x and f_y by $\boldsymbol{C}$, or rather by its eigenvectors $\boldsymbol{w}_\parallel(\psi)$ and $\boldsymbol{w}_\perp(\psi)$, induces an anisotropic behaviour which effects the proposed invariance.

Further, by replacing the regularised step function H_ε in Equation 15 with the identity function, the matrix $\boldsymbol{C}$ degenerates to

$$\frac{1}{\pi} \int_0^{2\pi} 1 \cdot \boldsymbol{e}_\varphi \boldsymbol{e}_\varphi^\top \, \mathrm{d}\varphi \;=\; \frac{1}{\pi} \begin{pmatrix} \pi & 0 \\ 0 & \pi \end{pmatrix} \;=\; \boldsymbol{I} \,. \tag{28}$$

The resulting data term coincides with the gradient constancy assumption in Equation 27. Hence, the census-based method may be regarded as a *censorisation* of the gradient constancy. On the one hand, this censorisation decreases the amount of extracted image information due to the binary quantisation of the directional derivative values. On the other hand, however, the induced anisotropy increases the robustness under illumination changes. While the original gradient constancy assumption is solely invariant w.r.t. global additive illumination changes, the *censored* gradient constancy assumption provides an invariance against any kind of monotonically increasing grey level rescalings.

4 Generalisation to Higher Order

The gained insights and in particular the continuous formulation of the census transform offer a natural generalisation of census-based data terms to higher order. For this purpose, let us replace the first order directional derivative $\boldsymbol{e}_\varphi^\top \boldsymbol{\nabla} f$ in constraint (4) by its second order counterpart

$$\boldsymbol{e}_\varphi^\top \boldsymbol{\mathcal{H}}(f) \boldsymbol{e}_\varphi \,, \tag{29}$$

where $\boldsymbol{\mathcal{H}}(f)$ represents the spatial 2×2 Hessian of f. Then the second order census-based constancy assumption reads

$$H\!\left(\boldsymbol{e}_\varphi^\top \boldsymbol{\mathcal{H}}(f(x{+}u,\ y{+}v,\ t{+}1))\boldsymbol{e}_\varphi\right) \;-\; H\!\left(\boldsymbol{e}_\varphi^\top \boldsymbol{\mathcal{H}}(f(x,y,t))\boldsymbol{e}_\varphi\right) \;\overset{!}{=}\; 0 \,, \tag{30}$$

with $\varphi \in [0, 2\pi)$. Again, regularising the Heaviside step function H allows to linearise the first term around $(x, y, t)^\top$, which finally leads to

$$H_\varepsilon'(\boldsymbol{e}_\varphi^\top \boldsymbol{\mathcal{H}}(f)\boldsymbol{e}_\varphi) \cdot \boldsymbol{e}_\varphi^\top \big(\underbrace{\boldsymbol{\mathcal{H}}(f_x) \cdot u + \boldsymbol{\mathcal{H}}(f_y) \cdot v + \boldsymbol{\mathcal{H}}(f_t)}_{\boldsymbol{P}_{uv}}\big)\boldsymbol{e}_\varphi \;\overset{!}{=}\; 0 \,. \tag{31}$$

The matrix $\boldsymbol{\mathcal{H}}(f_x) \cdot u + \boldsymbol{\mathcal{H}}(f_y) \cdot v + \boldsymbol{\mathcal{H}}(f_t)$ represents the constancy assumption of the Hessian [30]. In the following, we will abbreviate it by $\boldsymbol{P}_{uv}$. With this abbreviation, the quadratic second order census-based data term is given by

$$M_2(u, v) \;:=\; \frac{1}{\pi} \int_0^{2\pi} H_\varepsilon'^{\,2}(\boldsymbol{e}_\varphi^\top \boldsymbol{\mathcal{H}}(f)\boldsymbol{e}_\varphi) \cdot \big(\boldsymbol{e}_\varphi^\top \boldsymbol{P}_{uv} \boldsymbol{e}_\varphi\big)^2 \, \mathrm{d}\varphi \,. \tag{32}$$

4.1 Anisotropy

Contrary to the first order data term, an isolation of a census tensor is not obvious in the second order case. However, an interpretation of the second order census-based data term is still possible on a more abstract level: For small ε, the factor $H_\varepsilon'^2(e_\varphi^\top \mathcal{H}(f)e_\varphi)$ vanishes for all second order directional derivatives with an absolute value somewhat larger than 0. In contrast, a second order directional derivative close to 0 induces a very large weight. It corresponds to a constant part or to an inflection point of the one-dimensional function along the considered direction e_φ. Solely in those directions, we assume the constancy of the second order directional derivative to be valid. In fact, $e_\varphi^\top \mathcal{H}(f)e_\varphi$ remains there zero for all rescalings that do not change the sign of the image curvature, e.g. affine rescalings with a positive slope. However, in contrast to the first order census, the invariance w.r.t. *any* kind of monotonically increasing rescalings is lost.

4.2 Uncensored Version

Analogously to the first order data term, let us now replace the Heaviside step function in Equation 32 by the identity function. It is not very hard to verify that

$$\frac{1}{\pi} \int_0^{2\pi} 1 \cdot \left(e_\varphi^\top \boldsymbol{P}_{uv} e_\varphi\right)^2 \mathrm{d}\varphi \;=\; \frac{1}{2} \cdot \|\boldsymbol{P}_{uv}\|_F^2 \;+\; \frac{1}{4} \cdot \mathrm{tr}^2(\boldsymbol{P}_{uv}), \tag{33}$$

where $\|.\|_F$ denotes the Frobenius norm and tr is the trace operator. The first term $\|\boldsymbol{P}_{uv}\|_F^2$ represents the quadratic data term of the linearised Hessian constancy assumption, while the second term $\mathrm{tr}^2(\boldsymbol{P}_{uv})$ is identical to the quadratic data term of the linearised Laplacian constancy assumption; see Papenberg et al. [30]. Thus, the second order census-based method may be regarded as a censorisation of those two assumptions. While the Hessian and Laplacian are solely invariant under additive changes, their censored version also provides an invariance w.r.t. affine rescalings with positive slope.

5 Implementation

For the ease of implementation, we cast the linearised constancy assumption from (7) into the versatile *motion tensor* framework of Bruhn [4]. To this end, we exploit the equivalence

$$H_\varepsilon'\left(e_\varphi^\top \boldsymbol{\nabla} f\right) \cdot e_\varphi^\top \boldsymbol{p}_{uv} \;=\; \begin{pmatrix} \partial_x H_\varepsilon\left(e_\varphi^\top \boldsymbol{\nabla} f\right) \\ \partial_y H_\varepsilon\left(e_\varphi^\top \boldsymbol{\nabla} f\right) \\ \partial_t H_\varepsilon\left(e_\varphi^\top \boldsymbol{\nabla} f\right) \end{pmatrix}^\top \begin{pmatrix} u \\ v \\ 1 \end{pmatrix}. \tag{34}$$

Furthermore, we approximate the periodic integral in Equation 9 by the Riemann sum and finally obtain

$$M(u,v) \;=\; \begin{pmatrix} u \\ v \\ 1 \end{pmatrix}^\top \boldsymbol{J} \begin{pmatrix} u \\ v \\ 1 \end{pmatrix}, \tag{35}$$

with the motion tensor

$$\boldsymbol{J} \;=\; \frac{2}{N} \sum_{n=0}^{N-1} \begin{pmatrix} \partial_x H_\varepsilon\left(e_{\varphi_n}^\top \boldsymbol{\nabla} f\right) \\ \partial_y H_\varepsilon\left(e_{\varphi_n}^\top \boldsymbol{\nabla} f\right) \\ \partial_t H_\varepsilon\left(e_{\varphi_n}^\top \boldsymbol{\nabla} f\right) \end{pmatrix} \begin{pmatrix} \partial_x H_\varepsilon\left(e_{\varphi_n}^\top \boldsymbol{\nabla} f\right) \\ \partial_y H_\varepsilon\left(e_{\varphi_n}^\top \boldsymbol{\nabla} f\right) \\ \partial_t H_\varepsilon\left(e_{\varphi_n}^\top \boldsymbol{\nabla} f\right) \end{pmatrix}^\top. \tag{36}$$

Here, N denotes the number of considered neighbours and $\varphi_n := 2\pi \frac{n}{N}$. Choosing e.g. $N=8$, the eight direct neighbours of each pixel are used to compute the census signatures. Generally, we assume the images to be sampled on a regular grid with horizontal and vertical grid sizes h_1 and h_2, respectively. Accordingly, the directional derivative $\boldsymbol{e}_{\varphi_n}^\top \boldsymbol{\nabla} f$ at pixel $(i, j)^\top$ is approximated via the two point stencil

$$\left[\boldsymbol{e}_{\varphi_n}^\top \boldsymbol{\nabla} f\right]_{i,j} \; = \; \frac{[f]_{i+d_1, j+d_2} - [f]_{i,j}}{\sqrt{(h_1 d_1)^2 + (h_2 d_2)^2}} \, , \tag{37}$$

where the vector $\boldsymbol{d} := (d_1, d_2)^\top \neq \boldsymbol{0}$ represents, especially for diagonal neighbours, a scaled version of $\boldsymbol{e}_{\varphi_n}$ (cf. Section 2.1). All other spatial and temporal derivatives are computed by means of standard finite differences.

The implementation of the second order census-based approach is also straightforward. The corresponding motion tensor reads

$$\frac{2}{N} \sum_{n=0}^{N-1} \begin{pmatrix} \partial_x H_\varepsilon \big(\boldsymbol{e}_{\varphi_n}^\top \boldsymbol{\mathcal{H}}(f) \boldsymbol{e}_{\varphi_n}\big) \\ \partial_y H_\varepsilon \big(\boldsymbol{e}_{\varphi_n}^\top \boldsymbol{\mathcal{H}}(f) \boldsymbol{e}_{\varphi_n}\big) \\ \partial_t H_\varepsilon \big(\boldsymbol{e}_{\varphi_n}^\top \boldsymbol{\mathcal{H}}(f) \boldsymbol{e}_{\varphi_n}\big) \end{pmatrix} \begin{pmatrix} \partial_x H_\varepsilon \big(\boldsymbol{e}_{\varphi_n}^\top \boldsymbol{\mathcal{H}}(f) \boldsymbol{e}_{\varphi_n}\big) \\ \partial_y H_\varepsilon \big(\boldsymbol{e}_{\varphi_n}^\top \boldsymbol{\mathcal{H}}(f) \boldsymbol{e}_{\varphi_n}\big) \\ \partial_t H_\varepsilon \big(\boldsymbol{e}_{\varphi_n}^\top \boldsymbol{\mathcal{H}}(f) \boldsymbol{e}_{\varphi_n}\big) \end{pmatrix}^\top , \tag{38}$$

where the second order directional derivatives are calculated by the term

$$\left[\boldsymbol{e}_{\varphi_n}^\top \boldsymbol{\mathcal{H}}(f) \boldsymbol{e}_{\varphi_n}\right]_{i,j} \; = \; \frac{[f]_{i+2d_1, j+2d_2} - 2\,[f]_{i+d_1, j+d_2} + [f]_{i,j}}{(h_1 d_1)^2 + (h_2 d_2)^2} \, , \tag{39}$$

In both cases (first and second order), the resulting discrete versions of the Euler-Lagrange equations create a sparse linear system of equations, which we solve iteratively using a variant of the Gauß-Seidel method, namely successive over-relaxation [47].

6 Evaluation

To illustrate the impact of the different data terms in Table 1, we conduct our experiments on an image sequence with a simple motion pattern; see Figure 3. Further, we subject the grey values $g \in [0, 255]$ of the second input image to the monotonically increasing transformation

$$g_{\text{out}} \; = \; 255 \cdot \left(\frac{m \cdot g_{\text{in}} + a}{255}\right)^\gamma , \tag{40}$$

where the constant a represents additive changes, $m > 0$ multiplicative changes and $\gamma > 0$ is used for gamma manipulations (cf. Figure 4, *first row*).

The parameter ε of the regularised step function can be adapted to the noise level and is here fixed to 10^{-3}. Furthermore, the input images are presmoothed with a Gaussian of standard deviation 0.4 and the census signatures are determined on a 3×3 neighbourhood ($N=8$).

First image   Ground truth flow   Second image
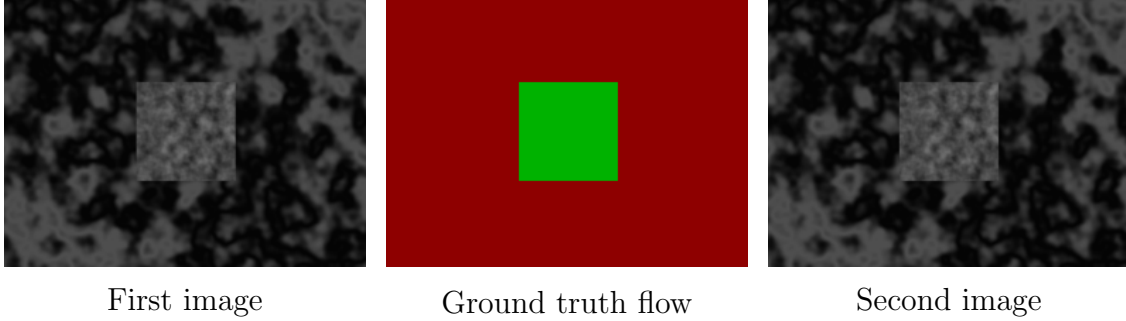
Figure 3: Input sequence. From the first to the second input image, the square is moving to the left while the background is shifted to the right. This motion is illustrated by the optic flow plot in the *middle*, where colour indicates the direction and brightness the amount of motion.

Table 1: Overview of the presented constancy assumptions, the corresponding linearised data terms and the invariances under intensity rescalings. As in the text, we use the abbreviations $\boldsymbol{p}_{uv} = \boldsymbol{\nabla} f_x \cdot u + \boldsymbol{\nabla} f_y \cdot v + \boldsymbol{\nabla} f_t$ and $\boldsymbol{P}_{uv} = \boldsymbol{\mathcal{H}}(f_x) \cdot u + \boldsymbol{\mathcal{H}}(f_y) \cdot v + \boldsymbol{\mathcal{H}}(f_t)$.

Constancy assumption	Linearised data term	Invariance
Gradient	$\|\boldsymbol{p}_{uv}\|_2^2$	additive
Census (1st order)	$\frac{1}{\pi} \int\limits_0^{2\pi} H_\varepsilon'^2(\boldsymbol{e}_\varphi^\top \boldsymbol{\nabla} f) \cdot \left(\boldsymbol{e}_\varphi^\top \boldsymbol{p}_{uv}\right)^2 \, \mathrm{d}\varphi$	monotonically increasing
Hessian and Laplacian	$\frac{1}{2} \cdot \|\boldsymbol{P}_{uv}\|_F^2 + \frac{1}{4} \cdot \mathrm{tr}^2(\boldsymbol{P}_{uv})$	additive
Census (2nd order)	$\frac{1}{\pi} \int\limits_0^{2\pi} H_\varepsilon'^2(\boldsymbol{e}_\varphi^\top \boldsymbol{\mathcal{H}}(f)\boldsymbol{e}_\varphi) \cdot \left(\boldsymbol{e}_\varphi^\top \boldsymbol{P}_{uv}\boldsymbol{e}_\varphi\right)^2 \mathrm{d}\varphi$	affine with positive slope
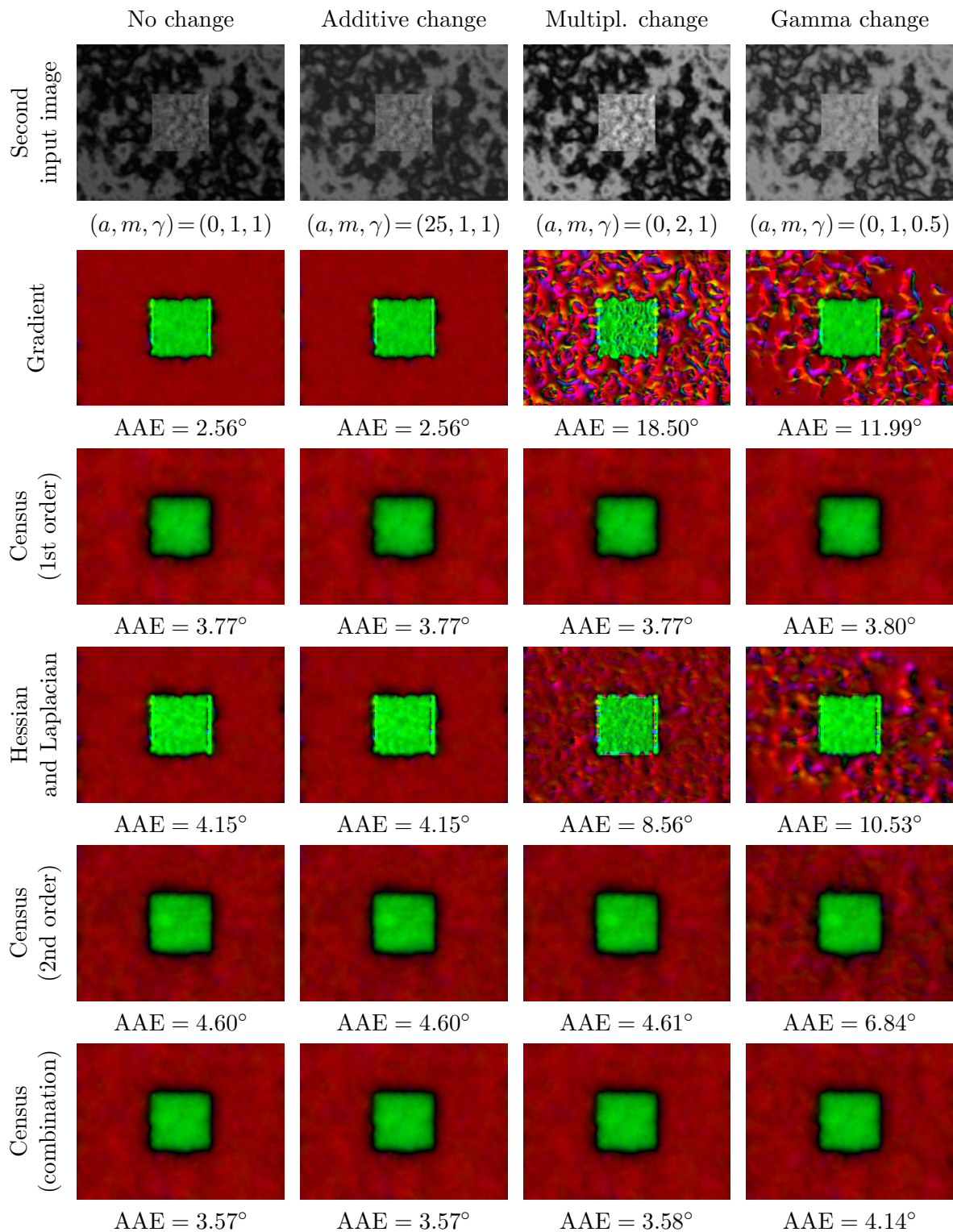
Figure 4: Visual comparison of the discussed constancy assumptions under illumination changes. The second input image (*first row*) is manipulated by different grey level rescalings (cf. Equation 40). Constancy assumptions from *second to last row*: gradient ($\alpha = 58$), 1st order census ($\alpha = 7$), Hessian and Laplacian ($\alpha = 55$), 2nd order census ($\alpha = 7$), and the combination of 1st and 2nd order census ($\alpha = 6$).

13
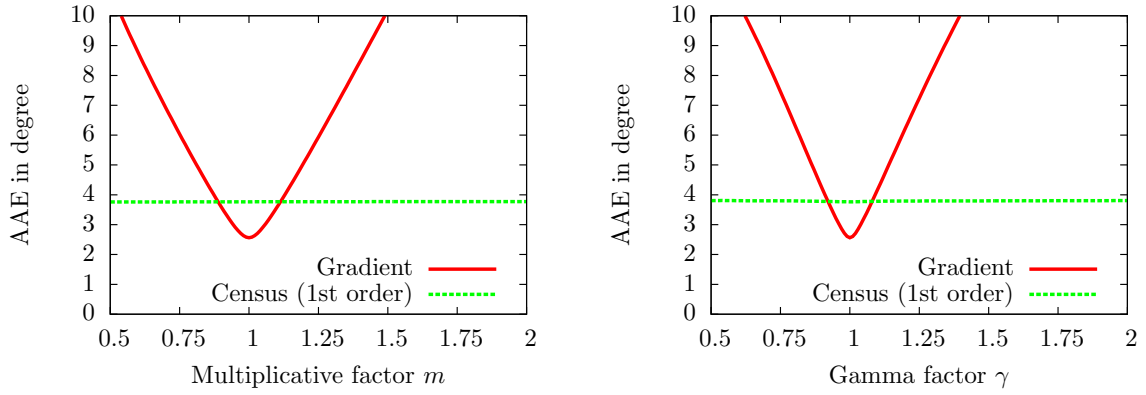
Figure 5: Comparison of the gradient constancy assumption and its censored version under global multiplicative illumination changes (*left*) and gamma manipulations (*right*). The parameter setting can be found in Figure 4.
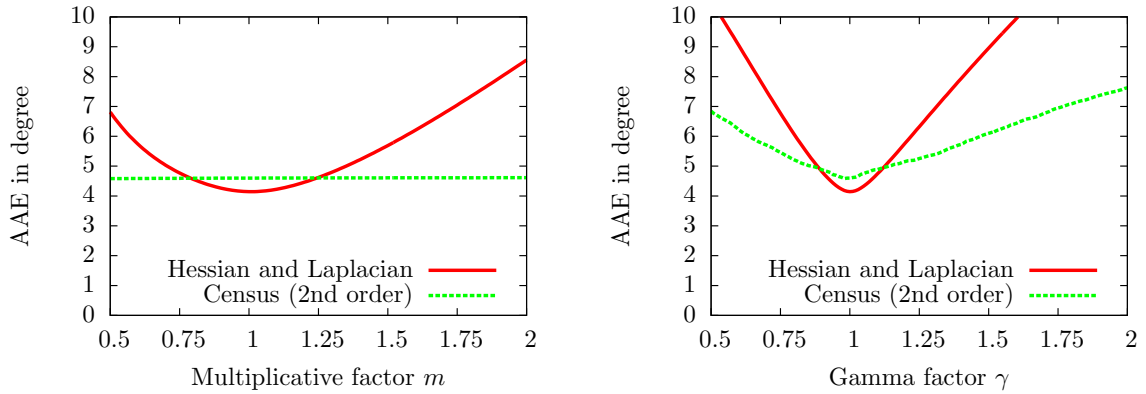
Figure 6: Comparison of the combined constancy assumption of the Hessian and the Laplacian as well as its censored version under global multiplicative illumination changes (*left*) and gamma manipulations (*right*). The parameter setting can be found in Figure 4.

6.1 First Order

Let us first investigate the first order census approach. The *second and third row* in Figure 4 demonstrate the increased robustness of the census-based method compared to the gradient constancy assumption. In the absence of artificial illumination changes (*first column*), the gradient constancy provides a better *average angular error* (AAE) [2]. It extracts more information form the input images. The resulting flow fields for additive changes (*second column*) remain unaltered due to the inherent invariance of both methods. In contrast, the gradient constancy assumption is not invariant under multiplicative rescalings and gamma manipulations (*third and fourth column*). However, the censored version provides an increased robustness. The absolute invariance is slightly affected due to the presmoothing and ε being unequal to zero.

The plots in Figure 5 confirm our observations: The gradient constancy is not able to compensate for multiplicative changes and gamma modifications. Contrary, the census-based approach provides the proposed robustness. However, there is no free lunch: The increase of robustness is associated with a loss of accuracy in the presence of small illumination changes.

6.2 Second Order

Similar observations apply to the second order approach. While the constancy assumption of the Hessian and the Laplacian is only valid under additive changes, its censored version shows also an invariance w.r.t. multiplicative changes. However, as discussed, an invariance against gamma modifications is not given; see Figure 4 (*fourth and fifth row*). Nonetheless, the plots in Figure 6 suggest the increased robustness of the censored approach under those gamma changes, compared to the constancy assumption of the Hessian and the Laplacian. Again, the invariance and increased robustness come at the price of a loss of accuracy in the case of small brightness variations.

Moreover, especially in the case of additive and multiplicative changes, a combination of the first and second order-based methods may be beneficial. In our example, we weight the first order term with 0.7 and the second order one with 0.3. In this way, we gain an increase in quality of 0.2° compared to standard first order census methods (cf. Figure 4, *last row*). These findings go along with the findings of Puxbaum and Ambrosch [32], who recommend to apply a modified version of the census transform to the image as well as to its first spatial derivatives.

7 Conclusions and Future Work

Research in recent years has demonstrated that some fairly simple concepts such as soft and hard thresholding or sparsity can be extremely powerful and theoretically interesting. The census transform can be seen as another representative along this line. By interpreting it in the continuous limit and embedding it into a variational framework we have shown two theoretical key properties: the strong reliance on local extrema as well as the restriction of the gradient constancy assumption along level lines. They exploit the morphological invariance of the gradient direction in a clever way and yield the observed robustness under illumination changes. This builds the basis for the success of the census

transform in the context of correspondence problems. Furthermore, the gained insights allow a natural generalisation of the census idea to higher order that is especially useful in the case of multiplicative illumination changes.

The key properties of the census transform are of course not restricted to optic flow models. Since they have already proven to be equally beneficial for stereo reconstruction [21] and face detection [9], we want to test their applicability for further computer vision tasks such as the registration of exposure sequences in future work.

Our findings confirm the general usefulness of studying continuous limits of inherently discrete morphological transforms. Other examples include e.g. continuous reinterpretations of median filters in terms of mean curvature motion [12] and morphological amoebae as self-snakes [46].

Acknowledgements

A   Proofs

The proofs below are based on the sketches from [45] and provide full mathematical details and adaptations to our specific situation. For didactic reasons, we replace the symmetric function $H_\varepsilon'^2 \colon \mathbb{R} \to \mathbb{R}_{>0}$ by an equivalent function g, only defined in $\mathbb{R}_{\geq 0}$. In contrast to [45], the family of functions in Theorem 2 is modified: Instead of $g(s) \leq \beta s^{-(1+\gamma)/2}$, we use $g(s) \leq \beta s^{-(1+\gamma)}$ for a suitable $\beta > 0$, $s > s_0 > 0$, and $\tilde{\gamma} \geq \gamma > 0$. Moreover, we substitute u_σ by the variable f, representing a smoothed version of the input image.

A.1   Eigendecomposition of Census Tensor

Theorem 1. *Let $g \colon \mathbb{R}_{\geq 0} \to \mathbb{R}_{>0}$ and let $\boldsymbol{e}_\varphi$ represent the unit vector $(\cos \varphi, \sin \varphi)^\top$. Furthermore, let $(r, \psi)^\top$ be the polar coordinates of $\boldsymbol{\nabla} f$. Then, for $\boldsymbol{\nabla} f \neq \boldsymbol{0}$ the orthonormal basis of the symmetric 2×2 census tensor*

$$\boldsymbol{C} \;=\; \frac{1}{\pi} \int_0^{2\pi} g(|\boldsymbol{e}_\varphi^\top \boldsymbol{\nabla} f|) \cdot \boldsymbol{e}_\varphi \boldsymbol{e}_\varphi^\top \, \mathrm{d}\varphi \tag{41}$$

is given by the normalised eigenvectors

$$\boldsymbol{w}_\parallel(\psi) \;=\; \frac{\boldsymbol{\nabla} f^\perp}{|\boldsymbol{\nabla} f|} \;=\; \begin{pmatrix} -\sin \psi \\ \cos \psi \end{pmatrix} \tag{42}$$

and

$$\boldsymbol{w}_\perp(\psi) \;=\; \frac{\boldsymbol{\nabla} f}{|\boldsymbol{\nabla} f|} \;=\; \begin{pmatrix} \cos \psi \\ \sin \psi \end{pmatrix}, \tag{43}$$

with corresponding eigenvalues

$$\lambda_\parallel(r) \;=\; \frac{4}{\pi} \int_0^{\pi/2} g(r \cdot \cos \varphi) \cdot \sin^2 \varphi \, \mathrm{d}\varphi \tag{44}$$

16

and

$$\lambda_\perp(r) \;=\; \frac{4}{\pi} \int_0^{\pi/2} g(r \cdot \cos\varphi) \cdot \cos^2\varphi \, \mathrm{d}\varphi \,. \tag{45}$$

Proof. Let us first analyse the matrix $\boldsymbol{C}$. The argument of the function g can be formulated in terms of the polar coordinates r and ψ of $\boldsymbol{\nabla} f$:

$$|\boldsymbol{e}_\varphi^\top \boldsymbol{\nabla} f| \;=\; |r \cdot \cos(\varphi - \psi)| \,. \tag{46}$$

Plugging this in Equation 41 yields

$$\boldsymbol{C} \;=\; \frac{1}{\pi} \int_0^{2\pi} g(|r \cdot \cos(\varphi - \psi)|) \cdot \boldsymbol{e}_\varphi \boldsymbol{e}_\varphi^\top \, \mathrm{d}\varphi \,. \tag{47}$$

Due to the symmetry and the π-periodicity of the integrand, the matrix may be rewritten as

$$\boldsymbol{C} \;=\; \frac{2}{\pi} \int_0^{\pi} g(|r \cdot \cos\varphi|) \cdot \boldsymbol{e}_{\varphi+\psi} \boldsymbol{e}_{\varphi+\psi}^\top \, \mathrm{d}\varphi \,. \tag{48}$$

Furthermore, the $\pi/2$-symmetry of the integrands in Equation 44 and 45 allow to write the eigenvalues as

$$\lambda_\|(r) \;=\; \frac{2}{\pi} \int_0^{\pi} g(|r \cdot \cos\varphi|) \cdot \sin^2\varphi \, \mathrm{d}\varphi \tag{49}$$

and

$$\lambda_\perp(r) \;=\; \frac{2}{\pi} \int_0^{\pi} g(|r \cdot \cos\varphi|) \cdot \cos^2\varphi \, \mathrm{d}\varphi \,. \tag{50}$$

Let us now consider the matrix-vector product $\left(\lambda_\|(r) \cdot \boldsymbol{I} - \boldsymbol{C} \right) \boldsymbol{w}_\|(\psi)$:

$$\frac{2}{\pi} \int_0^{\pi} g(|r \cdot \cos\varphi|) \cdot \begin{pmatrix} (\cos^2(\varphi+\psi) - \sin^2\varphi)\sin\psi & - & \cos(\varphi+\psi)\sin(\varphi+\psi)\cos\psi \\ \cos(\varphi+\psi)\sin(\varphi+\psi)\sin\psi & - & (\sin^2(\varphi+\psi) - \sin^2\varphi)\cos\psi \end{pmatrix} \, \mathrm{d}\varphi \,. \tag{51}$$

Expanding the trigonometric terms by means of the addition theorems and simplifying the result using the identity $\cos^2\psi + \sin^2\psi = 1$ leads to

$$\frac{-2}{\pi} \begin{pmatrix} \cos\psi \\ \sin\psi \end{pmatrix} \int_0^{\pi} g(|r \cdot \cos\varphi|) \cdot \cos\varphi \, \sin\varphi \, \mathrm{d}\varphi \,. \tag{52}$$

Due to the symmetry of the integrand with respect to $\pi/2$, the integral vanishes, i.e. $\left(\lambda_\|(r) \cdot \boldsymbol{I} - \boldsymbol{C} \right) \boldsymbol{w}_\|(\psi) = 0$. Hence, $\boldsymbol{w}_\|(\psi)$ is an eigenvector with the corresponding eigenvalue $\lambda_\|(r)$.

The eigenvectors of the symmetric matrix $\boldsymbol{C}$ set up an orthonormal system. Consequently, $\boldsymbol{w}_\perp(\psi) = \left(\boldsymbol{w}_\|(\psi) \right)^\perp$ is also an eigenvector. Further, since

$$\begin{aligned} \lambda_\|(r) + \lambda_\perp(r) \;&=\; \mathrm{tr}(\boldsymbol{C}) \\ &=\; \frac{2}{\pi} \int_0^{\pi} g(|r \cdot \cos(\varphi - \psi)|) \cdot (\sin^2\varphi + \cos^2\varphi) \, \mathrm{d}\varphi \\ &=\; \frac{2}{\pi} \int_0^{\pi} g(|r \cdot \cos\varphi|) \cdot (\sin^2\varphi + \cos^2\varphi) \, \mathrm{d}\varphi \end{aligned} \tag{53}$$

the corresponding eigenvalue $\lambda_\perp(r)$ is given by Equation 45. $\qquad\square$
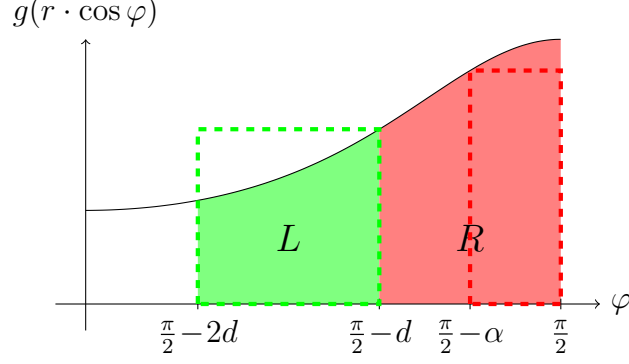
Figure 7: Illustration of the integrals $L(r, d)$ (green) and $R(r, d)$ (red). The dashed rectangles show the corresponding upper and lower bounds from Equation 58 and 59, respectively.

A.2 Ratio of Eigenvalues at High Contrast Edges

Theorem 2. *Let $g \colon \mathbb{R}_{\geq 0} \to \mathbb{R}_{>0}$ be a monotonically decreasing function with the limit $\lim_{s \to \infty} g(s) = 0$. Furthermore, $g(s) \leq \beta s^{-(1+\gamma)}$ for a suitable $\beta > 0$, $s > s_0 > 0$, and $\tilde{\gamma} \geq \gamma > 0$. Then, the ratio of the eigenvalues fulfils*

$$\lim_{r \to \infty} \frac{\lambda_{\parallel}(r)}{\lambda_{\perp}(r)} = \infty, \tag{54}$$

where $\lambda_{\parallel}(r)$ and $\lambda_{\perp}(r)$ represent the eigenvalues of the census tensor; see Theorem 1.

To prove this theorem, we first introduce the following lemma:

Lemma 1. *Let $0 < d \leq \frac{\pi}{4}$ and*

$$L(r, d) = \int_{\pi/2 - 2d}^{\pi/2 - d} g(r \cdot \cos \varphi) \, \mathrm{d}\varphi, \tag{55}$$

$$R(r, d) = \int_{\pi/2 - d}^{\pi/2} g(r \cdot \cos \varphi) \, \mathrm{d}\varphi. \tag{56}$$

Then, for $r > \frac{1}{\cos(\pi/2 - d)}$ the relation

$$\frac{L(r, d)}{R(r, d)} \leq 2 \frac{\beta}{g(1)} \left(\frac{d}{2} \right)^{-\gamma} r^{-\gamma} \tag{57}$$

holds.

Lemma 1. The term $\cos \varphi$ is decreasing for $\varphi \in [0, \pi/2]$, and as a result $g(r \cdot \cos \varphi)$ is monotonically increasing in φ. With $0 < \alpha \leq d$, the following inequalities hold (cf. Figure 7):

$$L(r, d) \leq d \cdot g(r \cdot \cos(\pi/2 - d)) \tag{58}$$

18

and

$$R(r, d) \geq \alpha \cdot g(r \cdot \cos(\pi/2 - \alpha)). \tag{59}$$

This further implies

$$\frac{L(r, d)}{R(r, d)} \leq \frac{d \cdot g(r \cdot \cos(\pi/2 - d))}{\alpha \cdot g(r \cdot \cos(\pi/2 - \alpha))}. \tag{60}$$

In the next step, we fix α to $\alpha_r = \pi/2 - \arccos(1/r)$, which is by definition in the range of 0 and d for the assumption $r > \frac{1}{\cos(\pi/2 - d)}$:

$$\frac{L(r, d)}{R(r, d)} \leq \frac{d \cdot g(r \cdot \cos(\pi/2 - d))}{\alpha_r \cdot g(1)}. \tag{61}$$

Furthermore, we use the estimate $\arccos x \leq \pi/2 - x$, $x \in [0, 1]$ to obtain

$$\alpha_r = \frac{\pi}{2} - \arccos \frac{1}{r} \geq \frac{1}{r}. \tag{62}$$

With $r \geq 1/\alpha_r$ this gives

$$\frac{L(r, d)}{R(r, d)} \leq \frac{d}{g(1)} r \cdot g(r \cdot \cos(\pi/2 - d)). \tag{63}$$

The assumption $g(s) \leq \beta s^{-(1+\gamma)}$ yields

$$\frac{L(r, d)}{R(r, d)} \leq \frac{d}{g(1)} \beta \cdot r^{-\gamma} \cdot \cos(\pi/2 - d)^{-(1+\gamma)}. \tag{64}$$

In the last step, we exploit the inequality $\cos(x) \geq \pi/4 - x/2$ for $x \in [0, \pi/2]$, i.e. in our particular case

$$\cos(\pi/2 - d) \geq \frac{d}{2}, \tag{65}$$

which finally leads to

$$\frac{L(r, d)}{R(r, d)} \leq 2 \frac{\beta}{g(1)} \left(\frac{d}{2}\right)^{-\gamma} r^{-\gamma}. \tag{66}$$

This concludes the proof of Lemma 1. $\qquad\square$

Now we are in a position to prove Theorem 2.

Proof. Due to

$$\lim_{r \to \infty} \frac{\lambda_\parallel(r)}{\lambda_\perp(r)} = \infty \quad \Leftrightarrow \quad \lim_{r \to \infty} \frac{\lambda_\parallel(r) + \lambda_\perp(r)}{\lambda_\perp(r)} = \infty, \tag{67}$$

it is equivalent to show that

$$\lim_{r \to \infty} \frac{\lambda_\perp(r)}{\lambda_\parallel(r) + \lambda_\perp(r)} = 0. \tag{68}$$

19

In the following, we make use of Lemma 1. To this end, let us introduce the variables

$$L_k = \int_{\phi_k}^{\phi_{k+1}} g(r \cdot \cos \varphi) \, \mathrm{d}\varphi \tag{69}$$

$$R_k = \int_{\phi_{k+1}}^{\pi/2} g(r \cdot \cos \varphi) \, \mathrm{d}\varphi \,, \tag{70}$$

where ϕ_k $(k = 0, 1, \dots)$ is defined by

$$\phi_k = \frac{\pi}{2} - \frac{\pi}{4} \left(\frac{1}{2} \right)^{k-1}. \tag{71}$$

The differences of both integration limits in (69) and (70) are given by

$$d_k = \phi_{k+1} - \phi_k = \frac{\pi}{4} \left(\frac{1}{2} \right)^k = \frac{\pi}{2} - \phi_{k+1}. \tag{72}$$

Applying Lemma 1 and using $r > \frac{1}{\cos(\pi/2 - d_k)}$ gives

$$\frac{L_k}{R_k} \leq 2 \frac{\beta}{g(1)} \left(\frac{d_k}{2} \right)^{-\gamma} r^{-\gamma} = 2 \frac{\beta}{g(1)} \left(\frac{8}{\pi} \right)^{\gamma} 2^{k\gamma} r^{-\gamma}. \tag{73}$$

Let us recall that $g(r \cdot \cos \varphi)$ is monotonically increasing for $\varphi \in [0, \pi/2]$. Thus, L_k and R_k are smaller or equal than R_0, for all k. With Equation 73, it follows for $r > \frac{1}{\cos(\pi/2 - d_k)}$ that

$$\frac{L_k}{R_0} \leq \frac{L_k}{R_k} \leq 2 \frac{\beta}{g(1)} \left(\frac{8}{\pi} \right)^{\gamma} 2^{k\gamma} r^{-\gamma}. \tag{74}$$

In the next steps, let us relate $\lambda_\perp(r)$ from Equation 45 to L_k and R_k. To this end, we write $\lambda_\perp(r)$ as the sum

$$\lambda_\perp(r) = \frac{4}{\pi} \left(\sum_{k=0}^{n} \int_{\phi_k}^{\phi_{k+1}} g(r \cdot \cos \varphi) \cdot \cos^2(\varphi) \, \mathrm{d}\varphi + \int_{\phi_{n+1}}^{\pi/2} g(r \cdot \cos \varphi) \cdot \cos^2(\varphi) \, \mathrm{d}\varphi \right), \tag{75}$$

where $n \in \mathbb{N}$. Since $\cos^2(x)$ is monotonically decreasing for $x \in [0, \pi/2]$, the following inequality holds:

$$\lambda_\perp(r) \leq \frac{4}{\pi} \left(\sum_{k=0}^{n} \left(\cos^2(\phi_k) \cdot \underbrace{\int_{\phi_k}^{\phi_{k+1}} g(r \cdot \cos \varphi) \, \mathrm{d}\varphi}_{L_k} \right) + \cos^2(\phi_{n+1}) \cdot \underbrace{\int_{\phi_{n+1}}^{\pi/2} g(r \cdot \cos \varphi) \, \mathrm{d}\varphi}_{R_n} \right). \tag{76}$$

Additionally, $\cos^2(x)$ is bounded by $\pi/2 - x$ for $x \in [0, \pi/2]$. Thus, with Equation 71 we can make the estimate:

$$\cos^2(\phi_k) \leq \frac{\pi}{2} \left(\frac{1}{2} \right)^k. \tag{77}$$

Using this inequality and exploiting that $R_k \leq R_0$ for all k results in

$$\lambda_\perp(r) \leq 2 \left(\sum_{k=0}^{n} \left(\frac{1}{2} \right)^k L_k + \left(\frac{1}{2} \right)^{n+1} R_0 \right). \tag{78}$$

20

Let us now analyse the expression $\frac{\lambda_\perp(r)}{\lambda_\|(r)+\lambda_\perp(r)}$ in Equation 68. To this end, we exploit the equality

$$
\begin{aligned}
\lambda_\|(r) + \lambda_\perp(r) &= \frac{4}{\pi} \int_0^{\pi/2} g(r \cdot \cos\varphi) \cdot (\cos^2(\varphi) + \sin^2(\varphi)) \, \mathrm{d}\varphi \\
&= \frac{4}{\pi} \left(\underbrace{\int_0^{\pi/4} g(r \cdot \cos\varphi) \, \mathrm{d}\varphi}_{L_0} + \underbrace{\int_{\pi/4}^{\pi/2} g(r \cdot \cos\varphi) \, \mathrm{d}\varphi}_{R_0} \right).
\end{aligned}
\tag{79}
$$

With Equation 78, it follows that

$$
\begin{aligned}
\frac{\lambda_\perp(r)}{\lambda_\|(r)+\lambda_\perp(r)} &\leq \frac{\pi}{2} \frac{\sum_{k=0}^n (1/2)^k L_k + (1/2)^{n+1} R_0}{L_0 + R_0} = \frac{\pi}{2} \frac{\sum_{k=0}^n (1/2)^k L_k/R_0 + (1/2)^{n+1}}{L_0/R_0 + 1} \\
&\leq \frac{\pi}{2} \left(\sum_{k=0}^n \left(\frac{1}{2}\right)^k \frac{L_k}{R_0} + \left(\frac{1}{2}\right)^{n+1} \right).
\end{aligned}
\tag{80}
$$

As we have seen, $\frac{L_k}{R_0}$ is bounded by Equation 74. This yields for all $r > \frac{1}{\cos(\pi/2 - d_n)}$ the estimate

$$
\frac{\lambda_\perp(r)}{\lambda_\|(r)+\lambda_\perp(r)} \leq \frac{\pi}{2} \left(2\frac{\beta}{g(1)} \left(\frac{8}{\pi}\right)^\gamma \sum_{k=0}^n \left(2^{\gamma-1}\right)^k \left(\frac{1}{r}\right)^\gamma + \left(\frac{1}{2}\right)^{n+1} \right).
\tag{81}
$$

Let now w.l.o.g. $\gamma \neq 1$. Then we can write the geometric sum as

$$
\sum_{k=0}^n \left(2^{\gamma-1}\right)^k = \frac{2^{(\gamma-1)(n+1)} - 1}{2^{\gamma-1} - 1} = \frac{2^{n\gamma+\gamma-n-1} - 1}{2^{\gamma-1} - 1}.
\tag{82}
$$

Further, with $1/r < \cos(\pi/2 - d_n) < 2^{-n}$ we obtain

$$
\frac{\lambda_\perp(r)}{\lambda_\|(r)+\lambda_\perp(r)} < \frac{\pi}{2} \left(2\frac{\beta}{g(1)} \left(\frac{8}{\pi}\right)^\gamma \frac{2^{\gamma-1-n} - 2^{-n\gamma}}{2^{\gamma-1} - 1} + \left(\frac{1}{2}\right)^{n+1} \right).
\tag{83}
$$

Finally, since γ is bounded

$$
\lim_{n \to \infty} \frac{\lambda_\perp(r)}{\lambda_\|(r)+\lambda_\perp(r)} = 0,
\tag{84}
$$

which further with $r > \frac{1}{\cos(\pi/2 - d_n)}$ implies Theorem 2. $\qquad \square$

References

[1] S. Baker, D. Scharstein, J. P. Lewis, S. Roth, M. J. Black, and R. Szeliski. A database and evaluation methodology for optical flow. *International Journal of Computer Vision*, 92(1):1–31, 2011.

[2] J. L. Barron, D. J. Fleet, and S. S. Beauchemin. Performance of optical flow techniques. *International Journal of Computer Vision*, 12(1):43–77, 1994.

[3] T. Brox, A. Bruhn, N. Papenberg, and J. Weickert. High accuracy optical flow estimation based on a theory for warping. In T. Pajdla and J. Matas, editors, *Computer Vision – ECCV 2004, Part IV*, volume 3024 of *Lecture Notes in Computer Science*, pages 25–36. Springer, Berlin, 2004.

[4] A. Bruhn. *Variational Optic Flow Computation: Accurate Modelling and Efficient Numerics.* PhD thesis, Dept. of Computer Science, Saarland University, Saarbrücken, Germany, 2006.

[5] M. Calonder, V. Lepetit, C. Strecha, and P. Fua. BRIEF: Binary robust independent elementary features. In K. Daniilidis, P. Maragos, and N. Paragios, editors, *Computer Vision – ECCV 2010, Part IV*, volume 6314 of *Lecture Notes in Computer Science*, pages 778–792. Springer, Berlin, 2010.

[6] N. Cornelius and T. Kanade. Adapting optical-flow to measure object motion in reflectance and X-ray image sequences. Technical Report 2502, Computer Science Department, Carnegie Mellon University, Pittsburgh, PA, 1983.

[7] D. Dederscheck, T. Müller, and R. Mester. Illumination invariance for driving scene optical flow using comparagram preselection. In *Proc. IEEE Intelligent Vehicles Symposium*, pages 742–747, Alcala de Henares, Spain, June 2012.

[8] O. Demetz, D. Hafner, and J. Weickert. The complete rank transform: A tool for accurate and morphologically invariant matching of structures. In T. Burghardt, D. Damen, W. Mayol-Cuevas, and M. Mirmehdi, editors, *Proc. 2013 British Machine Vision Conference*, Bristol, UK, Sept. 2013. BMVA Press.

[9] B. Fröba and A. Ernst. Face detection with the modified census transform. In *Proc. 6th IEEE International Conference on Automatic Face and Gesture Recognition*, pages 91–96, Seoul, Korea, 2004. IEEE Computer Society Press.

[10] A. Geiger, P. Lenz, C. Stiller, and R. Urtasun. Vision meets robotics: The KITTI dataset. *International Journal of Robotics Research*, 32:1229–1235, 2013.

[11] I. M. Gelfand and S. V. Fomin. *Calculus of Variations.* Dover, New York, 2000.

[12] F. Guichard and J.-M. Morel. Partial differential equations and image iterative filtering. In I. S. Duff and G. A. Watson, editors, *The State of the Art in Numerical Analysis*, number 63 in IMA Conference Series (New Series), pages 525–562. Clarendon Press, Oxford, UK, 1997.

[13] D. Hafner, O. Demetz, and J. Weickert. Why is the census transform good for robust optic flow computation? In A. Kuijper, T. Pock, K. Bredies, and H. Bischof, editors, *Scale-Space and Variational Methods in Computer Vision*, volume 7893 of *Lecture Notes in Computer Science*, pages 210–221. Springer, Berlin, 2013.

[14] G. D. Hager and P. N. Belhumeur. Real-time tracking of image regions with changes in geometry and illumination. In *Proc. IEEE Conference on Computer Vision and Pattern Recognition*, pages 403–410, San Francisco, CA, June 1996. IEEE Computer Society Press.

[15] H. W. Haussecker and D. J. Fleet. Computing optical flow with physical models of brightness variation. *IEEE Transactions on Pattern Analysis and Machine Intelligence*, 23(6):661–673, June 2001.

[16] G. Hermosillo, C. Chefd'Hotel, and O. Faugeras. Variational methods for multimodal image matching. *International Journal of Computer Vision*, 50(3):329–343, Dec. 2002.

[17] B. K. P. Horn and B. G. Schunck. Determining optical flow. *Artificial Intelligence*, 17:185–203, 1981.

[18] S. J. Kim and M. Pollefeys. Radiometric alignment of image sequences. In *Proc. IEEE Conference on Computer Vision and Pattern Recognition*, volume 1, pages 645–651, Washington, DC, June/July 2004. IEEE Computer Society Press.

[19] Y.-H. Kim and A. C. Kak. Error analysis of robust optical flow estimation by least median of squares methods for the varying illumination model. *IEEE Transactions on Pattern Analysis and Machine Intelligence*, 28(9):1418–1435, Sept. 2006.

[20] S. Mann. Comparametric equations with practical applications in quantigraphic image processing. *IEEE Transactions on Image Processing*, 9(8):1389–1406, Aug. 2000.

[21] X. Mei, X. Sun, M. Zhou, S. Jiao, H. Wang, and X. Zhang. On building an accurate stereo matching system on graphics hardware. In *Proc. IEEE International Conference on Computer Vision Workshops*, pages 467–474, Barcelona, Spain, Nov. 2011. IEEE Computer Society Press.

[22] Y. Mileva, A. Bruhn, and J. Weickert. Illumination-robust variational optical flow with photometric invariants. In F. A. Hamprecht, C. Schnörr, and B. Jähne, editors, *Pattern Recognition*, volume 4713 of *Lecture Notes in Computer Science*, pages 152–162. Springer, Berlin, 2007.

[23] M. A. Mohamed and B. Mertsching. TV-L1 optical flow estimation with image details recovering based on modified census transform. In G. Bebis, R. Boyle, B. Parvin, D. Koracin, C. Fowlkes, S. Wang, M.-H. Choi, S. Mantler, J. Schulze, D. Acevedo, K. Mueller, and M. Papka, editors, *Advances in Visual Computing, Part I*, volume 7431 of *Lecture Notes in Computer Science*, pages 482–491. Springer, Berlin, 2012.

[24] T. Müller, C. Rabe, J. Rannacher, U. Franke, and R. Mester. Illumination-robust dense optical flow using census signatures. In R. Mester and M. Felsberg, editors, *Pattern Recognition*, volume 6835 of *Lecture Notes in Computer Science*, pages 236–245. Springer, Berlin, 2011.

[25] T. Müller, J. Rannacher, C. Rabe, and U. Franke. Feature- and depth-supported modified total variation optical flow for 3D motion field estimation in real scenes. In *Proc. 24th IEEE Conference on Computer Vision and Pattern Recognition*, pages 1193–1200, Colorado Springs, CO, 2011. IEEE Computer Society Press.

[26] H.-H. Nagel. Displacement vectors derived from second-order intensity variations in image sequences. *Computer Vision, Graphics and Image Processing*, 21(1):85–117, Jan. 1983.

[27] S. Negahdaripour. Revised definition of optical flow: Integration of radiometric and geometric cues for dynamic scene analysis. *IEEE Transactions on Pattern Analysis and Machine Intelligence*, 20(9):961–979, Sept. 1998.

[28] T. Ojala, M. Pietikäinen, and D. Harwood. A comparative study of texture measures with classification based on featured distributions. *Pattern Recognition*, 29(1):51–59, 1996.

[29] G. Panin. Mutual information for multi-modal, discontinuity-preserving image registration. In G. Bebis, R. Boyle, B. Parvin, D. Koracin, C. Fowlkes, S. Wang, M.-H. Choi, S. Mantler, J. Schulze, D. Acevedo, K. Mueller, and M. Papka, editors, *Advances in Visual Computing, Part II*, volume 7432 of *Lecture Notes in Computer Science*, pages 70–81. Springer, Berlin, 2012.

[30] N. Papenberg, A. Bruhn, T. Brox, S. Didas, and J. Weickert. Highly accurate optic flow computation with theoretically justified warping. *International Journal of Computer Vision*, 67(2):141–158, Apr. 2006.

[31] M. Pietikäinen, A. Hadid, G. Zhao, and T. Ahonen. *Computer Vision Using Local Binary Patterns*. Springer, London, 2011.

[32] P. Puxbaum and K. Ambrosch. Gradient-based modified census transform for optical flow. In G. Bebis, R. Boyle, B. Parvin, D. Koracin, R. Chung, R. Hammoud, M. Hussain, T. Kar-Han, R. Crawfis, D. Thalmann, D. Kao, and L. Avila, editors, *Advances in Visual Computing, Part I*, volume 6453 of *Lecture Notes in Computer Science*, pages 437–448. Springer, Berlin, 2010.

[33] C. Rabe. *Detection of Moving Objects by Spatio-Temporal Motion Analysis: Real-time Motion Estimation for Driver Assistance Systems*. Südwestdeutscher Verlag für Hochschulschriften, Saarbrücken, Germany, 2012.

[34] R. Ranftl, S. Gehrig, T. Pock, and H. Bischof. Pushing the limits of stereo using variational stereo estimation. In *IEEE Intelligent Vehicles Symposium*, pages 401–407, Alcala de Henares, Spain, 2012. IEEE Computer Society Press.

[35] L. I. Rudin, S. Osher, and E. Fatemi. Nonlinear total variation based noise removal algorithms. *Physica D*, 60(1–4):259–268, Nov. 1992.

[36] C. Schnörr. On functionals with greyvalue-controlled smoothness terms for determining optical flow. *IEEE Transactions on Pattern Analysis and Machine Intelligence*, 15(10):1074–1079, 1993.

[37] F. Stein. Efficient computation of optical flow using the census transform. In C. E. Rasmussen, H. H. Bülthoff, M. A. Giese, and B. Schölkopf, editors, *Pattern Recognition*, volume 3175 of *Lecture Notes in Computer Science*, pages 79–86. Springer, Berlin, 2004.

[38] F. Steinbrücker, T. Pock, and D. Cremers. Advanced data terms for variational optic flow estimation. In M. A. Magnor, B. Rosenhahn, and H. Theisel, editors, *Proc. Vision, Modeling, and Visualization Workshop*, pages 155–164, Braunschweig, Germany, Nov. 2009. DNB.

[39] O. Tretiak and L. Pastor. Velocity estimation from image sequences with second order differential operators. In *Proc. Seventh International Conference on Pattern Recognition*, pages 16–19, Montreal, Canada, July 1984.

[40] S. Uras, F. Girosi, A. Verri, and V. Torre. A computational approach to motion perception. *Biological Cybernetics*, 60:79–87, 1988.

[41] J. van de Weijer and T. Gevers. Robust optical flow from photometric invariants. In *Proc. International Conference on Image Processing*, volume 3, pages 1835–1838, Singapore, Oct. 2004. IEEE Signal Processing Society.

[42] P. Viola and W. M. Wells III. Alignment by maximization of mutual information. *International Journal of Computer Vision*, 24(2):137–154, Sept. 1997.

[43] C. Vogel, S. Roth, and K. Schindler. An evaluation of data costs for optical flow. In J. Weickert, M. Hein, and B. Schiele, editors, *Pattern Recognition*, volume 8142 of *Lecture Notes in Computer Science*, pages 343–353. Springer, Berlin, 2013.

[44] A. Wedel, T. Pock, C. Zach, H. Bischof, and D. Cremers. An improved algorithm for TV-L1 optical flow. In D. Cremers, B. Rosenhahn, A. L. Yuille, and F. R. Schmidt, editors, *Statistical and Geometrical Approaches to Visual Motion Analysis*, volume 5604 of *Lecture Notes in Computer Science*, pages 23–45. Springer, Berlin, 2009.

[45] J. Weickert. Anisotropic diffusion filters for image processing based quality control. In A. Fasano and M. Primicerio, editors, *Proc. Seventh European Conference on Mathematics in Industry*, pages 355–362. Teubner, Stuttgart, 1994.

[46] M. Welk, M. Breuß, and O. Vogel. Morphological amoebas are self-snakes. *Journal of Mathematical Imaging and Vision*, 39(2):87–99, 2011.

[47] D. M. Young. *Iterative Solution of Large Linear Systems*. Academic Press, New York, 1971.

[48] R. Zabih and J. Woodfill. Non-parametric local transforms for computing visual correspondence. In J.-O. Eklundh, editor, *Computer Vision – ECCV '94*, volume 801 of *Lecture Notes in Computer Science*, pages 151–158. Springer, Berlin, 1994.